ADVANCED FUNCTIONAL MATERIALS
www.afm-journal.de

Evaluation of Entropy-Stabilized $(Mg_{0.2}Co_{0.2}Ni_{0.2}Cu_{0.2}Zn_{0.2})O$ Oxides Produced via Solvothermal Method or Electrospinning as Anodes in Lithium-Ion Batteries

Claudia Triolo, Wenlei Xu, Beatrix Petrovičovà, Nicola Pinna, and Saveria Santangelo**

Entropy-stabilized oxides (ESOs), such as $(Mg_{0.2}Co_{0.2}Ni_{0.2}Cu_{0.2}Zn_{0.2})O$, have recently gained significant interest as novel anodes for lithium-ion batteries (LIBs) due to their stable crystal structure and robust lithium-storage properties. In this work, $(Mg_{0.2}Co_{0.2}Ni_{0.2}Cu_{0.2}Zn_{0.2})O$ oxides with different morphologies are prepared by electrospinning and solvothermal method and are applied as anode active materials for LIBs. It is found that different morphologies possess different characteristics, namely particle size, particle size range, and defect density, which have a significant effect on the electrochemical behavior. The most active (Mg, Co, Ni, Cu, Zn) ESO shows outstanding electrochemical properties in terms of high reversible capacity (480 mAh g^{-1} at 20 mA g^{-1}), superior rate capability (206 mAh g^{-1} at 2 A g^{-1}), and excellent cycling stability (390 mAh g^{-1} at 500 mA g^{-1} after 300 cycles). The strategy demonstrates the importance of engineering microstructures in tailoring the electrochemical performance.

1. Introduction

Entropy-stabilized materials (ESMs) represent a recently emerged fascinating research field, gathering huge scientific attention. ESMs, also known as high-entropy materials (HEMs), consist in multicomponent solid solutions containing at least five cations in near-equimolar proportions, randomly distributed in the lattice.[1,2] This class of materials owes its name to the compensation of an unfavorable enthalpy of formation by the positive entropy of formation. Ideally, the stability of an elemental mixture in the form of a solid solution depends on Gibbs free energy, $\Delta G_{mix} = \Delta H_{mix} - T\Delta S_{conf}$, where ΔH_{mix} stands for the enthalpy of the mixture, T is the absolute temperature and ΔS_{conf} denotes the configurational entropy.[3,4] As ΔS_{conf} increases, ΔG_{mix} decreases and the solid solution becomes more stable.[5,6] $\Delta S_{conf} = -R\sum_{i=1}^{N} x_i \ln(x_i)$, with R denoting the ideal gas constant, is influenced by the number (N) of the mixture components and by their molar fractions (x_i).[7,8] For a given N, ΔS_{conf} reaches the maximum value, $R\ln(N)$, when the molar fractions of all components are the same. In real systems, nonideal interactions among components/elements can lead to short-or long-range ordering that decreases the overall ΔS_{conf}. Long-range ordering can be minimized by mixing isostructural components or elements having a similar charge.[5]

The ESM family includes alloys,[1,2] oxides,[9] and other composites,[10–15] which exhibit a variety of structures (rock-salt, spinel, perovskite, fluorite...) and are endowed with enhanced properties that make them very promising candidates for a very wide range of applications, spanning from catalysis[16–24] to energy conversion and storage.[25–38]

Rock-salt $(Mg_{0.2}Co_{0.2}Ni_{0.2}Cu_{0.2}Zn_{0.2})O$ was the first single-phase multicomponent oxide successfully synthesized, in 2015, via solid-state reaction from an equimolar mixture of MgO, CoO, NiO, CuO, and ZnO.[9] Since then, it has received very great attention and has been the focus of extensive research work.[21,25,33–37,39,40] Zhang et al.[40] have shown that its magnetic structure, long-range antiferromagnetically ordered below 113 K, consists of ferromagnetic sheets in the (111) planes with spins antiparallel between two neighboring planes, similar to nickel (II) and cobalt (II) oxides, whereas Usharani et al.[41] have reported that nanocrystalline (Mg, Co, Ni, Cu, Zn) ESO, due to smaller crystallite size and increased number of defect states, exhibits a "core–shell" magnetic behavior arising from the uncompensated or canted spin at the surface. According to Bérardan et al., the introduction of aliovalent elements in the (Mg, Co, Ni, Cu, Zn) ESO lattice leads to the obtainment of materials with colossal dielectric constants.[42] Liu et al.[21] have reported that defective high entropy (Mg, Co, Ni, Cu, Zn) oxide exhibits superior intrinsic activity toward the oxygen evolution reaction, whereas

C. Triolo, B. Petrovičovà, S. Santangelo
Dipartimento di Ingegneria Civile
dell'Energia, dell'Ambiente e dei Materiali (DICEAM)
Università "Mediterranea"
Loc. Feo di Vito, 89122 Reggio Calabria, Italy
E-mail: saveria.santangelo@unirc.it

C. Triolo, S. Santangelo
National Reference Center for Electrochemical Energy Storage (GISEL)
Consorzio Interuniversitario Nazionale per la Scienza e Tecnologia dei Materiali (INSTM)
50121 Firenze, Italy

W. Xu, N. Pinna
Institut für Chemie and IRIS Adlershof
Humboldt-Universität zu Berlin
Brook-Taylor Str. 2, 12489 Berlin, Germany
E-mail: nicola.pinna@hu-berlin.de

The ORCID identification number(s) for the author(s) of this article can be found under https://doi.org/10.1002/adfm.202202892.

DOI: 10.1002/adfm.202202892

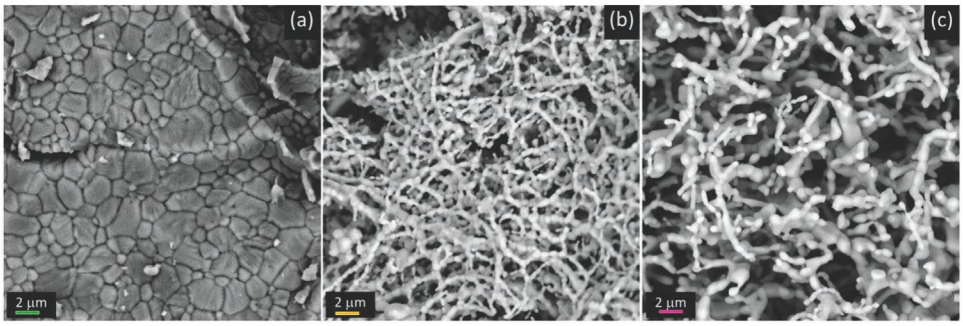

Figure 1. SEM images of samples a) 5MBsg, b) 5MBa and c) 5MBb.

Feng et al.[22] have shown "ultra-high" catalytic activity of holey lamellar (Mg, Co, Ni, Cu, Zn) ESO with the mesoporous structure for the solvent-free aerobic oxidation of benzyl alcohol.

In the field of electrochemical energy storage systems, the successful use of high entropy (Mg, Co, Ni, Cu, Zn) oxide has been demonstrated for all lithium-ion batteries (LIBs) components. Wang et al.[30] have prepared multianionic and multicationic high-entropy oxyhalides cathodes for rechargeable batteries by using $(Mg_{0.2}Co_{0.2}Ni_{0.2}Cu_{0.2}Zn_{0.2})O$ as the precursor. The family of $(MgCoNiCuZn)_{1-x-y}Ga_yA_xO$ solid-state electrolytes (where A stands for Li or Na) has been shown to exhibit "superionic" and fast ionic mobilities for Li^+ and Na^+.[29] The superior lithium-storage properties of $(Mg_{0.2}Co_{0.2}Ni_{0.2}Cu_{0.2}Zn_{0.2})O$-based anodes have been pointed out by many groups.[25,32–37] It has been proposed that Co^{2+}, Ni^{2+}, Cu^{2+} and Zn^{2+} cations are involved in the lithiation of (Mg, Co, Ni, Cu, Zn) ESO through the reaction $MO + 2\ Li^+ + 2\ e^- \rightarrow M + Li_2O$,[33] whereas Mg^{2+}, electrochemical inactive in the probed potential window, preserves the rock-salt structure during lithiation, by alleviating the degree of volume expansion and cracking of the electrode, restraining the agglomeration of active nanograins and reducing the degree of their pulverization.[33,34,36]

Different from carbon-based materials, exhibiting a relatively low capacity, and from high-capacity silicon-based materials, which suffer pulverization due to large volume variation, ESOs offer the advantage of simultaneously possessing high specific capacity and long cyclic stability.[25]

Solid-state reaction, requiring high temperatures (≥1000 °C[34,36]) and long heat treatments (typically 12–24 h[34,36]) is most frequently employed to prepare $(Mg_{0.2}Co_{0.2}Ni_{0.2}Cu_{0.2}Zn_{0.2})O$.[25,33,34,36] (Mg, Co, Ni, Cu, Zn) ESO exhibiting outstanding electrochemical property has also been produced by different methods (e.g., nebulized spray pyrolysis,[25] which is operated analogously at high temperature). Alternative methods have also been proposed for its preparation, e.g., microwave-assisted synthesis.[35] Very recently, electrospinning, a cost-effective technique widely used for the synthesis of high aspect ratio nanostructures for energy storage applications,[43–47] has been employed by Su et al.[37] to prepare single-phase $(Mg_{0.2}Co_{0.2}Ni_{0.2}Cu_{0.2}Zn_{0.2})O$ nanofibers (NFs) exhibiting stable long-term cyclability as a LIBs anode material.

This work focuses on the preparation of (Mg, Co, Ni, Cu, Zn) ESO through two different synthesis routes, solvothermal method (ST) and electrospinning (ES). Both routes allow for the production of pure single-phase HEOs under milder conditions (shorter heat treatments at lower temperatures) than solid-state techniques, which limit both the environmental impact and the detrimental effects of sintering on the oxide particle size. Moreover, both ST and ES can be scaled up and, hence, are suitable for large-scale sustainable manufacturing of LIBs electrode materials. Two polymers (polyvinylpyrrolidone, PVP, and polyacrylonitrile, PAN) are evaluated for the ESO production via ES. The as-calcined products are characterized and tested as anode materials in LIBs. The results are comparatively discussed to identify factors playing a crucial role on the electrochemical properties.

2. Results and Discussion

2.1. Morphology

Figures 1 and **2** and Figures S1–S4 (Supporting Information) summarize the results of the scanning electron microscopy/energy-dispersive X-ray spectroscopy (SEM/EDX) and high-resolution transmission electron microscopy (HRTEM)/EDX analyses on the produced samples. SEM micrographs demonstrate that our synthesis routes lead to the formation of ESOs with different morphologies (Figure 1 and Figure S1, Supporting Information). After calcination, the sample prepared via the ST reaction (5MBsg, Figure 1a and Figure S1a,b, Supporting Information) looks as constituted by aggregates of loosely bound particles with broadly distributed size. The particles (Figure 2a,d,g), having rounded/polyhedral shape with rounded vertices, easily detach from each other. By using the ES technique and PVP as a polymer (sample 5MBa, Figure 1b and Figure S1c,d, Supporting Information), an architecture is obtained containing both particle aggregates and filamentous structures with broadly distributed diameters (100–1400 nm). The filaments are built up by interconnected single particles (Figure 2b,e,h), similarly to what is shown by other authors for electrospun $(Mg_{0.2}Co_{0.2}Ni_{0.2}Cu_{0.2}Zn_{0.2})O$ NFs obtained by different precursors.[37] Fibers with a similar "segmented" structure[48] have been observed also in the case of electrospun zinc oxide NFs calcined at the same temperature (900 °C). The shape of the NF-composing particles is roughly similar to that observed in the sample produced via ST method. The distribution of the NF diameters, as estimated by the image analysis software, is centered at 510 nm (inset of Figure S1c, Supporting Information). By the use of PAN (sample 5MBb, Figure 1c and Figure S1e,f, Supporting Information), a denser 3D network is

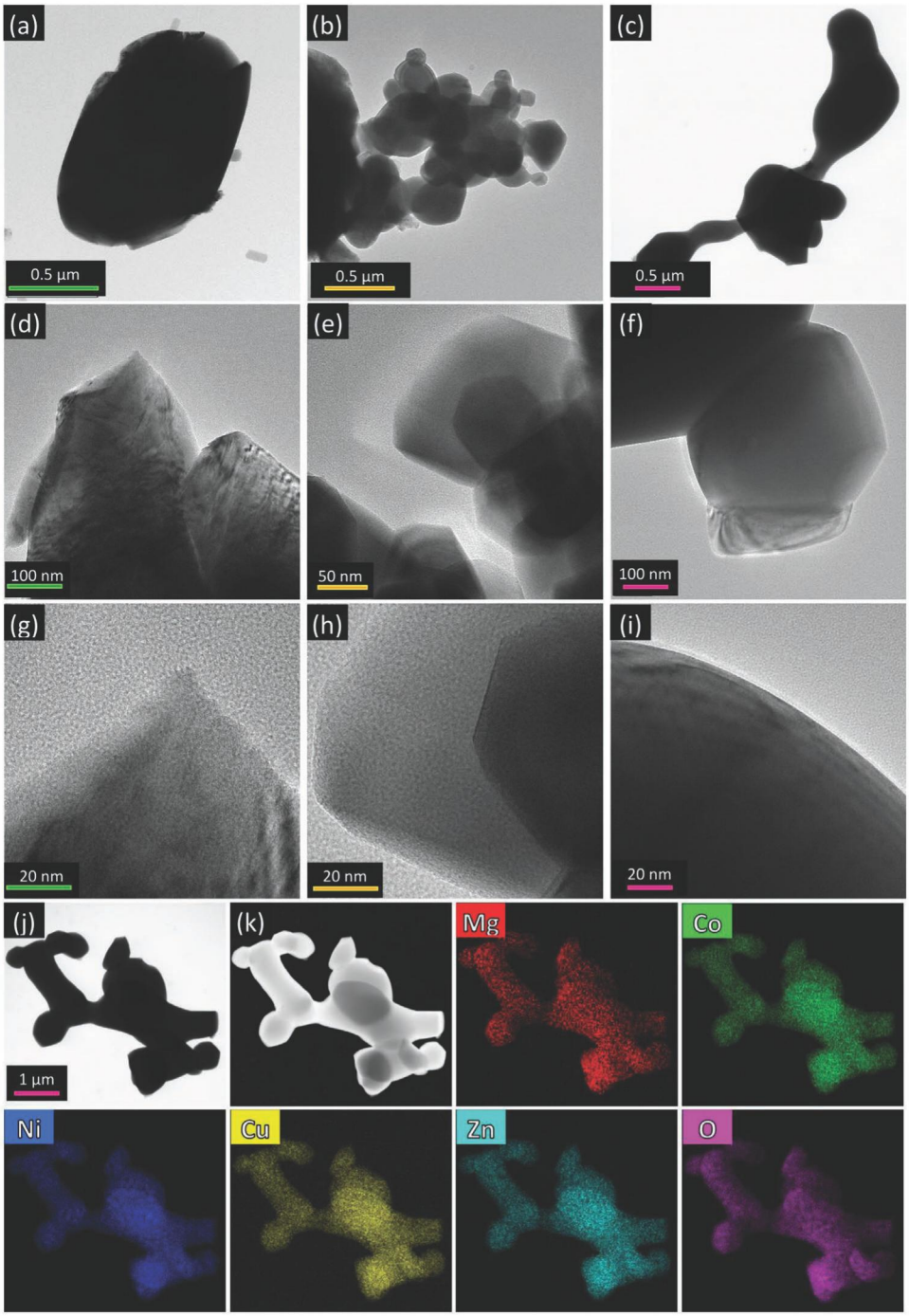

Figure 2. Results of the TEM and HRTEM/STEM/EDX analyses on samples a,d,g) 5MBsg, b,e,h) 5MBa and c,f,i) 5MBb. j,k) STEM/EDX elemental maps of sample 5MBb.

formed, made up by thicker fibers. Their diameters vary in a broader range (180–2500 nm), with the distribution centered on a larger value (720 nm, see inset of Figure S1e, Supporting Information). The fibers, resulting from the interconnection of particles with variable size and shape (Figure 2c), have a nonuniform diameter along their axis.

In sample 5MBsg, a very broad range of particle size is observed (0.1–9 µm), whereas in the electrospun ESOs the particle sizes vary in narrower ranges (0.2–2 µm and 0.1–1.5 µm for samples 5MBb and 5MBa, respectively). As a general trend, the mean ESO particle size decreases in the order 5MBsg (2 µm) >5MBb (0.65 µm) >5MBa (0.5 µm). The most homogeneous size distribution pertains to the electrospun sample derived from PVP (Figure S2, Supporting Information).

The elemental analyses by SEM/EDX and HRTEM/EDX (Figures S3 and S4, Supporting Information and Figure 2j,k)

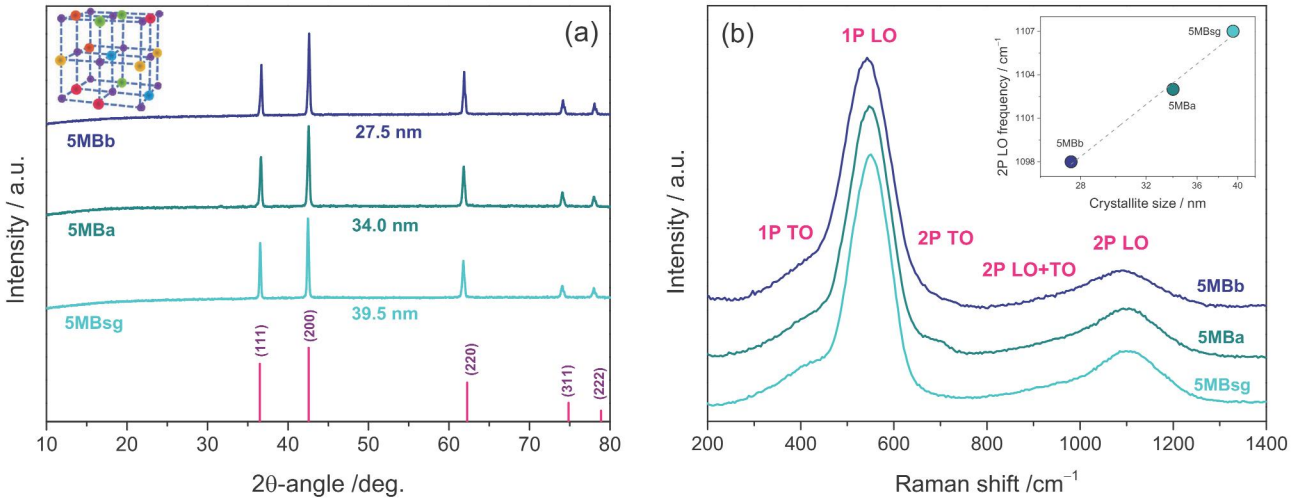

Figure 3. a) XRD patterns and b) averaged micro-Raman spectra of the investigated ESOs. Inset: frequency of 2P LO mode as a function of the average crystallite size, inferred from XRD analysis.

point to the absence of carbon residues in the calcined fibers: the organic constituents initially present in the samples completely degrade during the heat treatment. The elemental mapping evidence that, regardless of the synthesis pathway, Mg, Co, Ni, Cu, Ni, Zn, and O exhibit a spatially uniform distribution throughout the samples on both micro- and nanoscales (Figure S3d–f and Figure 2j,k, and Figure S4a–d, Supporting Information).

2.2. Crystalline Phase of the Oxide

Figure 3a compares the X-ray diffraction (XRD) patterns of the samples. Regardless of the synthesis method/conditions, five diffraction peaks are detected, at ca. 36.51°, 42.57°, 62.26°, 74.86°, and 78.88° 2θ-angles. They correspond to the reflections from the (111), (200), (220), (311), and (222) crystallographic planes of rock-salt structure, belonging to *Fm*-3*m* space group (JCPDS 47-1049).[21,31,35,49–52] No additional peaks attributable to segregation or secondary phases are observed, indicating that a pure single-phase solid solution is formed in all samples, namely $(Mg_{0.2}Co_{0.2}Ni_{0.2}Cu_{0.2}Zn_{0.2})O$. The average size of ESO crystallites, as estimated via the Scherrer formula from the most intense XRD peak, increases in the order 5MBb (27.5 nm) <5MBa (34.0 nm) <5MBsg (39.5 nm). These values indicate the polycrystalline nature of the ESOs.

Since the surface area of the region probed by micro-Raman spectroscopy (MRS, < 0.6 μm^2) is smaller than that probed by XRD, measuring Raman scattering from several random locations on each specimen allows for evaluating the spatial homogeneity of the samples (Figure S5, Supporting Information). Then, averaging the collected spectra provides a reliable picture of the entire sample (Figure 3b). The lack of significant differences in the spectral profiles relative to different locations in any sample confirms that a pure single-phase solid solution, without appreciable local deviations from the average chemical composition,[49] is formed regardless of the synthesis route. In sample 5MBsg (Figure S5a, Supporting Information), the change in the peak frequency from one random location to another never exceeds the spectral resolution (4 cm^{-1}). On the contrary, in samples 5MBa (Figure S5b, Supporting Information) and 5MBb (Figure S5c, Supporting Information), the position of the most intense peak in some locations is shifted slightly downwards/upwards from the average; this hints at the occurrence of local tensile/compressive strain. This behavior, more marked in the PAN-derived ESO, reflects in the inhomogeneous broadening of the main peak in the averaged spectra (Figure 3b).

Two one-phonon (1P) modes and three two-phonon (2P) modes are predicted for *Fm*-3*m* space group.[53–55] 1P modes include one transverse optical (TO) and one longitudinal optical (LO) mode, symmetry-forbidden in a perfect cubic lattice.[53,54] The detection of these modes is indicative of lattice distortion, defect-induced disorder, and surface effects.[41,53,54] 2P modes comprise the overtones of TO and LO modes and a combination band.[53–55] Accordingly, the averaged micro-Raman spectra were fitted to five Gaussian bands (Figure S6, Supporting Information). In the (Mg, Co, Ni, Cu, Zn)-ESO samples, the bands originating from 1P TO, 1P LO, 2P TO, 2P TO+LO and 2P LO modes are centered at 405–418 cm^{-1}, 543–551 cm^{-1}, 669–692 cm^{-1}, 913–935 cm^{-1} and 1098–1107 cm^{-1}, respectively.

The detection of a sharp 1P LO peak in all ESOs proves the presence of lattice distortion and structural disorder.[41,53,54] This finding is in line with reports on $(Mg_{0.2}Co_{0.2}Ni_{0.2}Cu_{0.2}Zn_{0.2})O$ particles produced by different techniques.[41] Moreover, in nickel oxide (NiO) nanoparticles, the intensity of 1P LO mode increases with increasing milling speed.[54] In the present case, the 1P LO peak intensifies with respect the 2P LO peak. The 1P-LO/2P-LO relative intensity increases in the order 5MBsg (2.7) < 5MBa (3.2) < 5MBb (3.9), that is in the opposite order with respect to the average size of the ESO crystallites. Moreover, the 2P LO mode shifts to lower frequency with the decreasing of the average crystallite size (inset of Figure 3b), analogously to what reported for NiO nanoparticles.[54]

Usharani et al.[41,53] have used the FWHM (full width at half maximum, ΔE) of the 1P LO peak to infer information of defect density in (Mg, Co, Ni, Cu, Zn)-ESO produced by a reverse co-precipitation process, flame spray pyrolysis and nebulized spray

pyrolysis. They have quantified the phonon lifetime (τ) via the uncertainty equation, $\tau = h/\Delta E$, where $h = 5.3 \times 10^{-12}$ cm^{-1} s is Planck's constant. Although for electrospun samples ΔE might be overestimated due to the inhomogeneous broadening of the peak, the τ values obtained (0.054, 0.049, and 0.047 ps for samples 5MBsg, 5MBa, and 5MBb, respectively, comparable to those reported by Usharani et al.[41]) point to an increase of the defect density in the order 5MBsg < 5MBa < 5MBb, in agreement with indications inferred from the XRD analysis.

Micro-Raman spectroscopy is a very sensitive technique able to detect even carbon traces.[56] No signal ascribable to carbon residues was detected in the Raman spectra of the calcined samples (Figure S7, Supporting Information). The very broad and weak peak detected near 1600 cm^{-1} is ascribed to two-magnon (2M) mode.[41] The detection of this band is indicative of the existence of antiferromagnetic state through the M^{2+}-O^{2-}-M'^{2+} superexchange interaction,[41,53–55] while its progressive disappearance points to the decrease of antiferromagnetic spin correlations.[55] In the present case, the intensity of the 2M-band decreases in the order 5MBsg > 5MBa > 5MBb, i.e., in the same order as crystal size, as expected.[55]

2.3. Electrochemical Properties

Electrochemical measurements of the (Mg, Co, NiCu, Zn) ESOs were carried out to evaluate the Li^+ storage properties in the potential window of 0.01–3.0 V (vs Li/Li^+). **Figure 4**a–c shows the cyclic voltammograms (CVs) of 5MBsg-, 5MBa-, and 5MBb-based electrodes in the initial five cycles at a scan rate of 0.1 mV s^{-1}. The similarity in shape of the three curves is indicative of the similar electrochemical behavior of the electrode materials and of the little role played by their morphologies. A strong peak centered at 0.4–0.6 V in the initial cathodic scan can be ascribed to the Co^{2+}/Co^0, Ni^{2+}/Ni^0, Cu^{2+}/Cu^0 and Zn^{2+}/Zn^0, reduction reactions, and the formation of both solid electrolyte interphase (SEI) layer and Li_2O.[33,34,36] While inactive Mg^{2+} cations should act as a stabilizing matrix, preserving the entire structural host during the de-/lithiation process.[25,33] The intensity of the strong peak is significantly reduced and shifts to higher potential at ≈1.2 V, which might be caused by the irreversible reaction of the first lithiation process and pulverization of the electrode materials.[33,36,57] There are two broad anodic peaks at around 0.8 and 1.8 V, which are related to

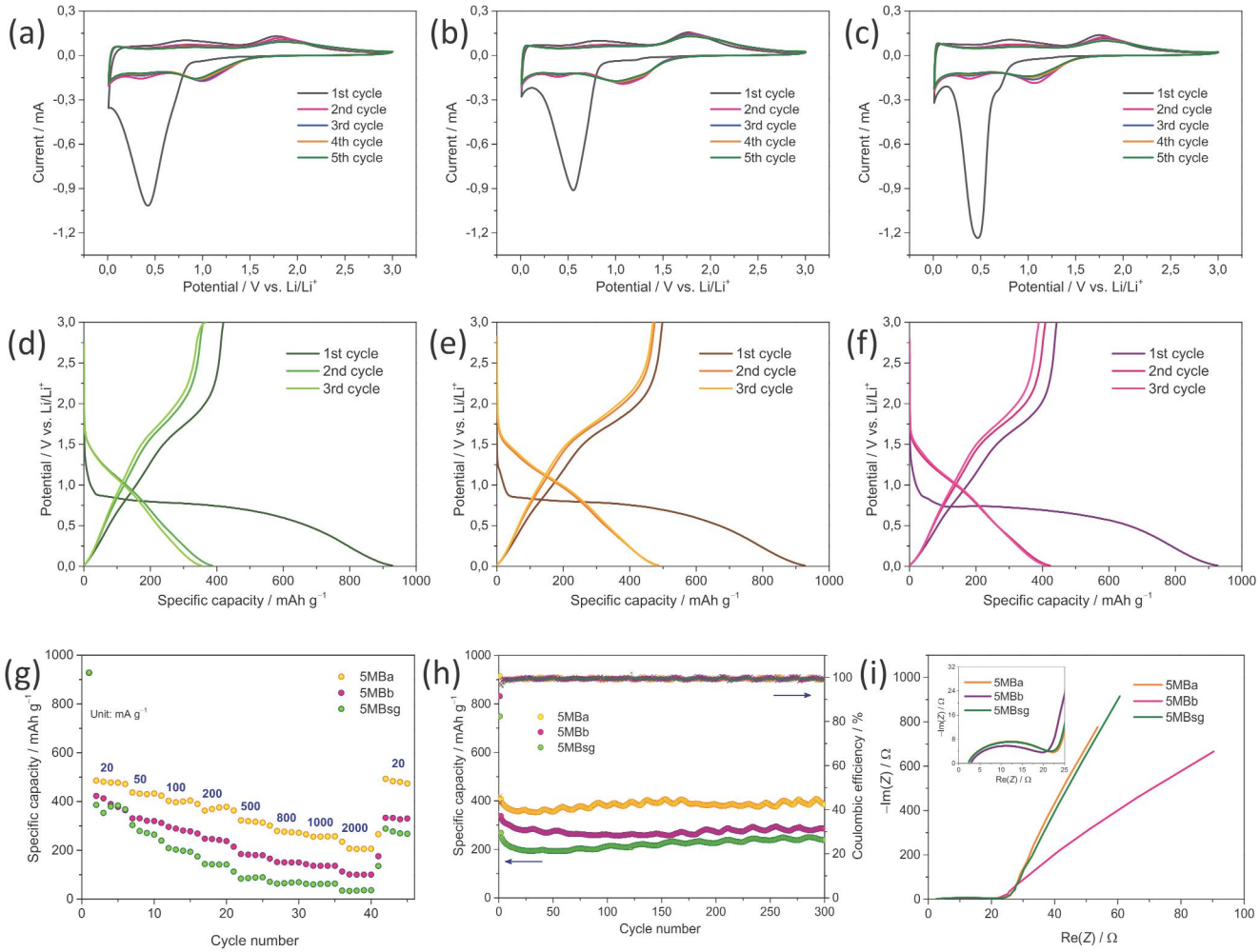

Figure 4. Electrochemical performance of the (Mg, Co, Ni, Cu, Zn) ESOs in the Li-ion half cells. a–c) CV curves (scanning rate of 0.1 mV s^{-1}) and d–f) galvanostatic charge–discharge curves measured at 20 mA g^{-1}; the shown data refer to samples a,d) 5MBsg, b,e) 5MBa, and c,f) 5MBb. g) Rate capability at different current densities, h) cycling stability at a current density of 500 mA g^{-1} and i) results of EIS measurements.

reoxidation of the reduced species produced during the lithiation process and decomposition of Li_2O.[33,34] In the subsequent cycles, both the reduction and oxidation peaks are overlapped, suggesting that the (Mg, Co, NiCu, Zn) ESO-based anodes exhibit good stability and reversibility for the Li^+ insertion and extraction reactions.

Figure 4d–f shows the initial three discharge–charge curves measured at 20 mA g^{-1}. In the first lithiation process, the typical voltage plateau at around 0.75 V corresponds to the reduction of transition metal oxides to metallic Co, Ni, Cu, and Zn, which is consistent with the CV results. The initial discharge/charge capacities for anodes 5MBsg, 5MBa and 5MBb are 928/420, 927/498, and 928/443 mAh g^{-1}, corresponding to initial Coulombic efficiencies (CEs) of 45.3%, 53.7%, 47.7%, respectively. The initial capacity loss is associated with the SEI formation due to the decomposition of the electrolyte and structural rearrangement.[33,58,30] The higher initial CE (77.5%) recently reported for electrospun (Mg, Co, Ni, Cu, Zn) ESO NFs produced from different precursors and heat treated under different conditions,[37] at the same rate (Table S1, Supporting Information), could be related with side reactions induced by the different electrolyte solvent and separator utilized. Interestingly, the initial discharge capacities for the three $(Mg_{0.2}Co_{0.2}Ni_{0.2}Cu_{0.2}Zn_{0.2})O$ anodes are almost the same, while the initial charge capacities are different. Their variation is in the opposite order as the mean ESO particle size, namely 5MBsg < 5MBb < 5MBa, in line with the widely agreed assessment that smaller particles showing larger areas of interface between the solid particle and the electrolyte can enhance capacity.[59] Besides, in the case of anodes 5MBa and 5MBb, fibrous structures offer direct current pathways along their axis and reduce the distance for the diffusion Li-ions, favoring capacity improvement.[37]

The rate capability and long-term stability of the (Mg, Co, Ni, Cu, Zn) ESO-based anodes were also evaluated. The results are shown in Figure 4g,h, respectively. As can be seen, in both kinds of tests, 5MBa outperforms both electrodes 5MBsg and 5MBb. Its lithiation capacities are 480, 432, 397, 369, 320, 276, 256, 206 mAh g^{-1} at 20, 50, 100, 200, 500, 1000, 2000 mA g^{-1}, respectively (Figure 4g). After the rate cycling, a reversible capacity of 484 mAh g^{-1} is recovered at 20 mA g^{-1}, implying its excellent reversibility. In addition, no obvious capacity fading is observed for anode 5MBa in the long-term stability test (Figure 4h). The capacity that is still delivered after 300 cycles at 500 mA g^{-1} (390 mAh g^{-1}) is higher than that reported for electrospun (Mg, Co, Ni, Cu, Zn) ESO NFs obtained under different preparation conditions[37] after the same number of cycles at lower rate (200 mA g^{-1}). Compared to the latter NFs,[37] also the rate capability of anode 5MBa is higher, e.g., at a rate of 1 A g^{-1}, it delivers 256 mAh g^{-1} against a value <200 mAh g^{-1}. However, much better results have been reported for (Mg, Co, Ni, Cu, Zn) ESO-based anodes produced by different techniques (Table S1, Supporting Information), which suggests that several factors still need to be optimized (i.e., synthesis conditions, but also electrode composition, type of electrolyte, binder, separator).

What immediately comes into view when looking at the results of the rate capability and long-term stability tests (Figure 4g,h, respectively) is that the performance of the three investigated anodes improves in the opposite order as the mean ESO particle size, namely 5MBsg < 5MBb < 5MBa, and that a greater improvement is achieved moving from sample 5MBb to sample 5MBa than from 5MBsg to 5MBb. These findings clearly point to the crucial role of the active material microstructure.

As shown in Figure S2 (Supporting Information), the (Mg, Co, Ni, Cu, Zn) ESO prepared by the ST method exhibits a broad range of particle sizes and larger average particle size, whereas the electrospun NFs consist of smaller particles, with narrower size distributions. Both PVP- and PAN-derived fibers have a "segmented" structure, but the latter, resulting from the interconnection of particles of more variable size and shape, have a less uniform diameter along their axis (compare Figure 1b,c). These features can reflect in different robustness of the electrode and stability of the SEI film, factors that have a synergistic influence on the overall performance of the battery.[60] In fact, it is widely recognized that a reduction of the particle size improves the mechanical performance of the electrode materials,[47] providing them with greater resistance to the large volume changes they suffer during the lithiation/delithiation process, particularly under high-rate conditions.[61] The wide size distribution of the active particles, in addition to influencing the Li^+-ion transport, leads to a heterogeneous current distribution and nonuniform lithiation both between particles and along the through-thickness direction.[61] Then, the broader particle size distribution, the more inhomogeneous the mechanical aging effect due to volume variations during charge and discharge. In turn, nonuniform mechanical aging (cracking and delamination) significantly reduces cycle life, energy density, and safety of the battery, especially at high rates.[61] Furthermore, as for the electrospun (Mg, Co, Ni, Cu, Zn) ESOs, it is well assessed that the NF network can accommodate severe volume variations, alleviating the high mechanical stress generated during cycling,[37,62] which is beneficial to the structural stability of the electrode. Therefore, the different microstructure of the three materials produced fully explains the observed differences in their electrochemical performance. The NF network, together with the smaller and more uniform size and shape of the particles that compose it, fully accounts for the better performance of sample 5MBa as an anode in LIBs.

Finally, Figure 4i shows the results of EIS measurements conducted to investigate the electrochemical kinetics of electrodes 5MBsg, 5MBa, and 5MBb. All Nyquist plots show a depressed semicircle in the high-to-medium frequency region and a straight line in the low-frequency region. The former is related to charge transfer resistance at the electrode/electrolyte interface, while the latter is associated with the Warburg impedance, which depends on the solid-state diffusion of Li^+-ions in the bulk electrode material. The high-frequency intercept at the *x*-axis is the bulk resistance of the electrolyte, separator, and electrode.[63] The behavior of 5MBb is different with respect to the remaining anodes, indicating that also the crystallinity matters. As expected,[64] the higher density of lattice defects in 5MBb results in increased Warburg impedance; the lower slope of the straight line in the low-frequency region hints at hindered Li^+ transport in the ESO electrode.[65]

2.4. ESO Stability

In order to ascertain the reversibility of the lithiation/de-lithiation process, ex situ Raman and XRD analyses were carried

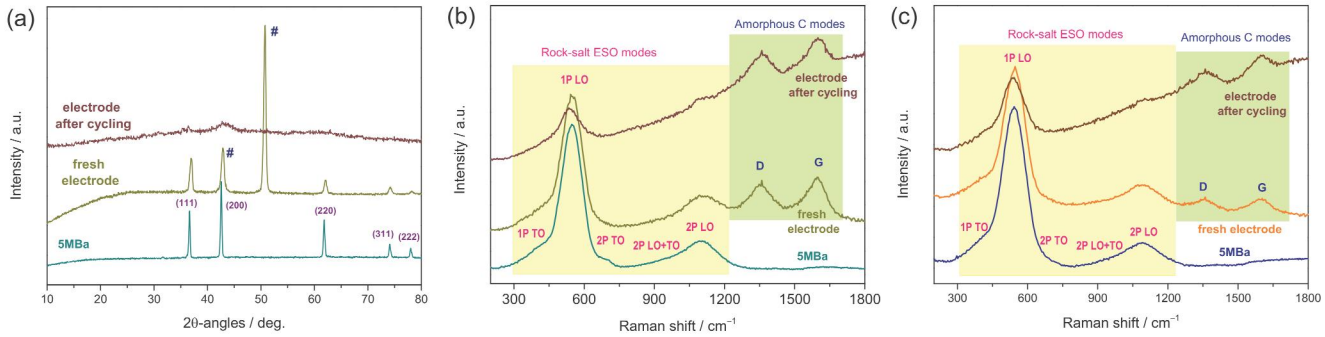

Figure 5. Results of a,b) MRS and c) XRD analyses on ESO-based electrodes, before and after cycling. The spectra of the pristine ESOs are also reported for comparison. The shown data refer to samples a,c) 5MBa- and b) 5MBb. In the diffractogram of fresh electrode, stars mark signals arising from the copper collector.

out on the $(Mg_{0.2}Co_{0.2}Ni_{0.2}Cu_{0.2}Zn_{0.2})O$-based anodes. Figure S8a,b (Supporting Information) display the micro-Raman spectra, measured at different random locations within each specimen. The averaged spectra, giving a picture of the sample bulk, are shown in **Figure 5**a,b. Regardless of the region probed by the laser spot, the fingerprint of the (Mg, Co, Ni, Cu, Zn) ESO is clearly visible in the Raman spectra below 1250 cm^{-1} (Figure S8a,b, Supporting Information) of both fresh and cycled electrodes, indicating that the insertion/extraction of Li^+ ions occurs without destroying the host ESO lattice.[66,67] In addition, the C sp^2 vibration modes originating from the carbonaceous Super P additive appear at higher frequencies (namely, D-band at 1350 cm^{-1} and G-band at 1580 cm^{-1}[66,67]). In some of the probed locations, only the most intense 1P LO peak is detected. The consequent increase of the 1P-LO/2P-LO relative intensity in the (averaged) spectra of the electrodes after cycling (Figure 5a,b) points to an increase of defect density.[54] Interestingly, after cycling, a noticeable broadening of the diffraction peaks is observed in the XRD pattern of the best performing sample (Figure 5c) pointing to a material amorphization. The formation of amorphous phases, because of their limited volume expansion,[68] seems to be helpful in preventing fractures,[69,70] thus favoring the electrode integrity and stability.

The specific capacities are still below the theoretical value for $(Mg_{0.2}Co_{0.2}Ni_{0.2}Cu_{0.2}Zn_{0.2})O$ (594 mAh g^{-1}[34]) and the values reported for some (Mg, Co, Ni, Cu, Zn) ESOs produced by different methods (Table S1, Supporting Information). Also the initial CE, which is a key parameter for the improvement of energy density in batteries, needs to be improved. Nonetheless, the possibility of obtaining pure single-phase (Mg, Co, Ni,Cu, Zn) ESOs under milder conditions than via solid-state reaction is here demonstrated. Moreover, this preliminary study provides a further contribution to the understanding of ESOs, which is of great importance since these materials can potentially be utilized for the development of all components of rechargeable Li^+ and Na^+ ion batteries.[25,29–31]

3. Conclusion

In this study, phase-pure rock-salt (Mg, Co, Ni, Cu, Zn) ESOs with three different morphologies have been successfully synthesized and tested as anodes in LIBs to identify the influence of the microstructure on the electrochemical properties. Physicochemical characterizations prove that the electrospun sample derived from PVP exhibits smaller particle size and narrower size- and shape distribution. These features provide larger contact area between electrolyte and active materials and shorten Li^+ diffusion length, leading to improved electrochemical kinetics, and reduced heterogeneity, which are beneficial to the structural stability of the electrode, particularly under high-rate conditions. The larger defect density of electrospun sample derived from PAN hinders the transport of Li^+. Electrochemical characterizations demonstrate that the PVP-derived sample delivers a large reversible capacity of 480 mAh g^{-1} at 20 mA g^{-1}, a high rate capability of 206 mAh g^{-1} at 2 A g^{-1}, and a high capacity retention of nearly 100% at 500 mA g^{-1} after 300 cycles. The outstanding electrochemical performance can be attributed to the synergistic effect of particle size, particle size distribution, and defect density. Moreover, the matrix of inactive Mg^{2+} cations also plays an important role in preserving rock-salt structure stability by buffering the volume change of the active material and restraining the agglomeration of electrochemically active nanograins. In addition, ex situ Raman and XRD analyses further demonstrate the reversibility of the lithiation/de-lithiation processes. Our microstructure-engineered strategy will be helpful for further exploring ESO electrode materials for energy storage applications.

4. Experimental Section

Reagents and Chemicals: For all syntheses of (Mg, Co, Ni, Cu, Zn)-ESO samples, the following reagents were utilized as metal sources: magnesium (II) acetate tetrahydrate, $Mg(CH_3COO)_2{\cdot}4H_2O$ (purity: 98%; CAS No. 16674-78-5, Sigma Aldrich), cobalt (II) acetate tetrahydrate, $Co(CH_3COO)_2{\cdot}4H_2O$ (purity: 99%; CAS No. 6147-53-1, Sigma Aldrich), nickel (II) acetate tetrahydrate, $Ni(CH_3COO)_2{\cdot}4H_2O$ (purity: 98%; CAS No. 6018-89-9, Sigma Aldrich), copper (II) acetate, $Cu(CH_3COO)_2$, (purity: 98%; CAS No. 142-71-2, Sigma Aldrich), zinc (II) acetate dihydrate, $Zn(CH_3COO)_2{\cdot}2H_2O$ (purity: 98%; CAS No. 5970-45-6, Fischer Scientific, Hampton, NH, USA). Table S2 (Supporting Information) reports the amounts needed in each synthesis to obtain ESOs with a nominal equiatomic composition of 20 at% Mg, Co, Ni, Cu, Ni, and Zn.

In addition, citric acid monohydrate, $HOC(COOH)(CH_2COOH)_2{\cdot}H_2O$ (purity: 98%; CAS No. 5949-29-1, Sigma Aldrich), was used as a complexing agent for the preparation of (Mg, Co, Ni, Cu, Zn)-ESO via solvothermal method (sample 5MBsg).

Two different combinations of polymer and solvent were evaluated for the preparation of ESO samples via electrospinning. Accordingly, a first sample (coded as 5MBa) was prepared by the use of polyvinylpyrrolidone, $(C_6H_9NO)_n$ (average molecular weight: 1 300 000 g mol^{-1}; purity: 98%; CAS No. 9003-39-8, Sigma Aldrich), as a polymer, and a solution containing ethanol, CH_3CH_2OH (purity: 99,5%; CAS No. 64-17-5, Sigma Aldrich), and N,N-dimethylformamide, $HCON(CH_3)_2$ (anhydrous: 99.8%; CAS No. 68-12-2, Sigma Aldrich), as a solvent. Polyacrylonitrile, $(C_3H_3N)_n$ (average molecular weight: 150 000 g mol^{-1}; purity: 99.9%; CAS No. 25014-41-9, Sigma Aldrich), and N,N-dimethylformamide respectively acted as a polymer and a solvent in the preparation of a second sample (coded as 5MBb).

Synthesis via Solvothermal Method: For the synthesis of sample 5MBsg via ST reaction, Mg, Co, Ni, Cu, Ni, and Zn salts were dissolved in 30 g water, one at a time. After stirring for 1 h, 3.4673 g citric acid (CA) was added and the resulting mixture was further stirred at 90 °C until a gel was formed. The as-obtained gel was dried at 80 °C overnight and, subsequently, calcined in static air at 350 °C for 2 h, at 500 °C for 2 h, at 800 °C for 2 h and finally at 900 °C for 2 h. As a result, powders consisting of ESO particles with rock-salt structure were obtained.

Syntheses via Electrospinning: Samples 5MBa and 5MBb were prepared by ES. In the former case, the spinnable solution was obtained by dissolving 0.5 g PVP in 2 g ethanol (EtOH) and 2.35 g *N*,*N*-dimethylformamide (DMF), whereas, in the latter, 0.325 g PAN was dissolved in 4.550 g DMF. Both solutions were stirred at room temperature (RT) until they became clear. Then, proper amounts of Mg, Co, Ni, Cu, Ni, and Zn salts (Table S2, Supporting Information) were added, one at a time, under continuous stirring.

The as-obtained homogeneous spinnable solution, containing a nominally equiatomic combination of Mg, Co, Ni, Cu, Ni and Zn, was loaded into a 20 mL syringe equipped with a 40 mm long 0.8 mm gauge stainless steel needle. ES was carried out by using a CH-01 Electrospinner 2.0 (Linari Engineering s.r.l.). The solution feeding rate, applied DC voltage and needle-collector distance were fixed at 23.5 µL min^{-1}, 15 kV and 11 cm, respectively. The NFs ejected from the needle were collected over an aluminum foil.

After drying at RT overnight to remove the solvent residuals, the as-spun nonwoven fibrous membrane was peeled from the collector and calcined in static air. A four-step heating process was operated in the case of sample 5MBa (350 °C for 2 h, 500 °C for 2 h, 800 °C for 2 h and 900 °C), while sample 5MBb was obtained through a two-step heat-treatment (700 °C for 2 h and 900 °C for 2 h). The obtained powders consisted of fibrous-like architectures built up by ESO NFs with rock-salt structure.

Physicochemical Characterization: The physicochemical properties of the produced ESOs were investigated by SEM, TEM, XRD, and MRS. A Phenom Pro-X scanning electron microscope equipped with an EDX spectrometer was utilized to acquire the SEM images and elemental maps. HRTEM, high-angle annular dark-field scanning transmission electron microscopy (HAADF-STEM), selected-area electron diffraction (SAED) and EDX elemental mappings were carried out on a FEI Talos F200S scanning/transmission electron microscope, operated at 200 kV.

XRD analysis was carried out with a Bruker D2 diffractometer using Ni β-filtered Cu-K_α radiation source (λ = 0.1541 nm). Micro-Raman analysis was conducted by using a NTEGRA—Spectra SPM NT-MDT confocal microscope coupled to a solid-state laser operating at 2.33 eV (532 nm). Raman scattering was measured in air at RT by using a low laser power (250 µW at the sample surface) to prevent local heating. The scattered light from the sample was collected by a 100X Mitutoyo objective (NA = 0.75), dispersed by a 600 lines mm^{-1} grating and detected by a cooled ANDOR iDus CCD Camera. Further details on the instrumentation can be found in reference.[71]

Electrochemical Characterization: Electrochemical properties of active materials (5MBa, 5MBb, and 5MBsg) were evaluated by using CR2032-type coin cells, which were assembled in an Ar-filled glovebox. First, 70% active materials, 20% conductive carbon black (Super P, Timcal) and 10% polyvinylidene fluoride (PVDF, Alfa Aesar) were homogeneously mixed with N-methyl-2-pyrrolidone (NMP, anhydrous 99.5%, Sigma-Aldrich). The resulting slurry was uniformly cast on Cu foil (Goodfellow, UK) with a doctor blade apparatus and then dried in a vacuum oven at 60 °C for 1 h. After a cold-laminating step, electrodes with a diameter of 12 mm were punched out and dried overnight at 120 °C under vacuum using a Büchi glass oven. The mass loading of active material is ≈ 1.5 mg cm^{-2}. Lithium metal foil was used as both counter and reference electrodes. 1 M $LiPF_6$ (ABCR, 99.9% battery grade) solution in a mixture of ethylene carbonate (EC, 99.9%, ABCR), diethyl carbonate (DEC, 99.9%, ABCR) and dimethyl carbonate (DMC, 99.9%, ABCR) with 1:1:1 volume ratio was used as the electrolyte. A glass microfiber filter (Whatman) was used as a separator.

Galvanostatic charge-discharge cycling was carried out at room temperature using a CT2001 A battery testing system (Landt Instruments). CVs were measured on a Bio-Logic VMP3 multichannel potentiostat/galvanostat with a built-in EIS analyzer. EIS was tested at open-circuit potential (OCP), in the frequency range of 100 kHz to 0.1 Hz with an amplitude of 10 mV.

Supporting Information

Supporting Information is available from the Wiley Online Library or from the author.

Acknowledgements

C.T. and W.X. contributed equally to this work. Christoph Erdmann is acknowledged for electron microscopy measurements. B.P. and S.S. gratefully thank the Italian Ministry of University and Research (MUR) for the financial support to this study through grant "PRIN 2017, 2017MCEEY4, Towards sustainable, high-performing, all-solid-state sodium-ion batteries." W.X. acknowledges the fellowship from the China Scholarship Council (CSC).

Open access funding enabled and organized by Projekt DEAL.

Conflict of Interest

The authors declare no conflict of interest.

Data Availability Statement

The data that support the findings of this study are available from the corresponding author upon reasonable request.

Keywords

entropy-stabilized oxides, lithium-ion batteries, rock-salt structures

Received: March 14, 2022
Revised: May 3, 2022
Published online:

[1] B. Cantor, I. T. H. Chang, P. Knight, A. J. B. Vincent, *Mater. Sci. Eng. A* **2004**, *375*, 213.
[2] J. W. Yeh, S. K. Chen, S. J. Lin, J. Y. Gan, T. S. Chin, T. T. Shun, C. H. T. Sau, S. Y. Chang, *Adv. Eng. Mater.* **2004**, *6*, 299.
[3] S. Akrami, P. Edalati, M. Fuji, K. Edalati, *Mater. Sci. Eng., R* **2021**, *146*, 100644.
[4] K. C. Pitike, S. Kc, M. Eisenbach, C. A. Bridges, V. R. Cooper, *Chem. Mater.* **2020**, *32*, 7507.

[5] S. J. McCormack, A. Navrotsky, *Acta Mater.* **2021**, *202*, 1.
[6] A. Sarkar, Q. Wang, A. Schiele, M. R. Chellali, S. S. Bhattacharya, D. Wang, T. Brezesinski, H. Hahn, L. Velasco, B. Breitung, *Adv. Mater.* **2019**, *31*, 1806236.
[7] Y. Ma, Y. Ma, Q. Wang, S. Schweidler, M. Botros, T. Fu, H. Hahn, T. Brezesinski, B. Breitung, *Energy Environ. Sci.* **2021**, *14*, 2883.
[8] G. M. Tomboc, T. Kwon, J. Joo, K. Lee, *J. Mater. Chem. A* **2020**, *8*, 14844.
[9] C. M. Rost, E. Sachet, T. Borman, A. Moballegh, E. C. Dickey, D. Hou, L. J. Jacob, S. Curtarolo, J. P. Maria, *Nat. Commun.* **2015**, *6*, 8485.
[10] J. Gild, Y. Zhang, T. Harrington, S. Jiang, T. Hu, M. C. Quinn, W. M. Mellor, N. Zhou, K. Vecchio, J. Luo, *Sci. Rep.* **2016**, *6*, 37946.
[11] T. Jin, X. Sang, R. R. Unocic, R. T. Kinch, X. Liu, J. Hu, H. Liu, S. Dai, *Adv. Mater.* **2018**, *30*, 1707512.
[12] R. Z. Zhang, F. Gucci, H. Zhu, K. Chen, M. J. Reece, *Inorg. Chem.* **2018**, *57*, 13027.
[13] E. Castle, T. Csanádi, S. Grasso, J. Dusza, M. Reece, *Sci. Rep.* **2018**, *8*, 8609.
[14] C. Oses, C. Toher, S. Curtarolo, *Nat. Rev. Mater.* **2020**, *5*, 295.
[15] R. Z. Zhang, M. J. Reece, *J. Mater. Chem. A* **2019**, *7*, 22148.
[16] G. Zhang, K. Ming, J. Kang, Q. Huang, Z. Zhang, X. Zheng, X. Bi, *Electrochim. Acta* **2018**, *279*, 19.
[17] R. Q. Yao, Y. T. Zhou, H. Shi, W. B. Wan, Q. H. Zhang, L. Gu, Y. F. Zhu, Z. Wen, X. Y. Lang, Q. Jiang, *Adv. Funct. Mater.* **2021**, *31*, 2009613.
[18] D. Feng, Y. Dong, P. Nie, L. Zhang, Z. A. Qiao, *Chem. Eng. J.* **2022**, *430*, 132883.
[19] T. X. Nguyen, Y. C. Liao, C. C. Lin, Y. H. Su, J. M. Ting, *Adv. Funct. Mater.* **2021**, *31*, 2101632.
[20] J. Hu, L. Cao, Z. Wang, J. Liu, J. Zhang, Y. Cao, Z. Lu, H. Cheng, *Compos. Commun.* **2021**, *27*, 100866.
[21] F. Liu, M. Yu, X. Chen, J. Li, H. Liu, F. Cheng, *Chin. J. Catal.* **2022**, *43*, 122.
[22] D. Feng, Y. Dong, L. Zhang, X. Ge, W. Zhang, S. Dai, Z. A. Qiao, *Angew. Chem.* **2020**, *132*, 19671.
[23] S. H. Albedwawi, A. AlJaberi, G. N. Haidemenopoulos, K. Polychronopoulou, *Mater. Des.* **2021**, *202*, 109534.
[24] Y. Gao, Y. Liu, H. Yu, D. Zou, *Appl. Catal., A* **2022**, *631*, 118478.
[25] A. Sarkar, L. Velasco, D. Wang, Q. Wang, G. Talasila, L. de Biasi, C. Kubel, T. Brezesinski, S. S. Bhattacharya, H. Hahn, B. Breitung, *Nat. Commun.* **2018**, *9*, 3400.
[26] A. Amiri, R. Shahbazian-Yassar, *J. Mater. Chem. A* **2021**, *9*, 782.
[27] M. Fu, X. Ma, K. Zhao, X. Li, D. Su, *iScience* **2021**, *24*, 102177.
[28] I. Hussain, C. Lamiel, M. Ahmad, Y. Chen, S. Shuang, M. S. Javed, Y. Yang, K. Zhang, *J. Energy Storage* **2021**, *44*, 103405.
[29] D. Bérardan, S. Franger, A. K. Meena, N. Dragoe, *J. Mater. Chem. A* **2016**, *4*, 9536.
[30] Q. Wang, A. Sarkar, D. Wang, L. Velasco, R. Azmi, S. S. Bhattacharya, T. Bergfeldt, A. Duvel, P. Heitjans, T. Brezesinski, H. Hahn, B. Breitung, *Energy Environ. Sci.* **2019**, *12*, 2433.
[31] Y. Chen, H. Fu, Y. Huang, L. Huang, X. Zheng, Y. Dai, Y. Huang, W. Luo, *ACS Mater. Lett.* **2020**, *3*, 160.
[32] H. Chen, N. Qiu, B. Wu, Z. Yang, S. Sun, Y. Wang, *RSC Adv.* **2019**, *9*, 28908.
[33] P. Ghigna, L. Airoldi, M. Fracchia, D. Callegari, U. Anselmi-Tamburini, P. D'angelo, N. Pianta, R. Ruffo, G. Cibin, D. Oliveira de Souza, E. Quartarone, *ACS Appl. Mater. Interfaces* **2020**, *12*, 50344.
[34] S. Y. Wang, T. Y. Chen, C. H. Kuo, C. C. Lin, S. C. Huang, M. H. Lin, C. C. Wang, H. Y. Chen, *Mater. Chem. Phys.* **2021**, *274*, 125105.
[35] M. Kheradmandfard, H. Minouei, N. Tsvetkov, A. K. Vayghan, S. F. Kashani-Bozorg, G. Kim, S. I. Hong, D. E. Kim, *Mater. Chem. Phys.* **2021**, *262*, 124265.
[36] N. Qiu, H. Chen, Z. Yang, S. Sun, Y. Wang, Y. Cui, *J. Alloys Compd.* **2019**, *777*, 767.
[37] J. Su, Z. Cao, Z. Jiang, G. Chen, Y. Zhu, L. Wang, G. Li, *Int. J. Appl. Ceram. Technol.* **2022**, https://doi.org/10.1111/ijac.14021.
[38] Y. Lin, N. Luo, M. Chamas, C. Hu, S. Grasso, *Int. J. Appl. Ceram. Technol.* **2021**, *18*, 1560.
[39] Z. Rak, C. M. Rost, M. Lim, P. Sarker, C. Toher, S. Curtarolo, J. P. Maria, D. W. Brenner, *J. Appl. Phys.* **2016**, *120*, 095105.
[40] J. Zhang, J. Yan, S. Calder, Q. Zheng, M. A. McGuire, D. L. Abernathy, Y. Ren, S. H. Lapidus, K. Page, R. P. Hermann, *Chem. Mater.* **2019**, *31*, 3705.
[41] N. J. Usharani, A. Bhandarkar, S. Subramanian, S. S. Bhattacharya, *Acta Mater.* **2020**, *200*, 526.
[42] D. Bérardan, S. Franger, D. Dragoe, A. K. Meena, N. Dragoe, *Phys. Status Solidi RRL* **2016**, *10*, 328.
[43] M. J. Laudenslager, R. H. Scheffler, W. M. Sigmund, *Pure Appl. Chem.* **2010**, *82*, 2137.
[44] Z. Dong, S. J. Kennedy, Y. Wu, *J. Power Sources* **2011**, *196*, 4886.
[45] G. Sun, L. Sun, H. Xie, J. Liu, *Nanomaterials* **2016**, *6*, 129.
[46] S. Peng, L. Li, J. K. Y. Lee, L. Tian, M. Srinivasan, S. Adams, S. Ramakrishna, *Nano Energy* **2016**, *22*, 361.
[47] S. Santangelo, *Appl. Sci.* **2019**, *9*, 1049.
[48] A. Senthamizhan, B. Balusamy, Z. Aytac, T. Uyar, *CrystEngComm* **2016**, *18*, 6341.
[49] J. Dąbrowa, M. Stygar, A. Mikuła, A. Knapik, K. Mroczka, W. Tejchman, M. Danielewski, M. Martin, *Mater. Lett.* **2018**, *216*, 32.
[50] A. Kumar, G. Sharma, A. Aftab, M. I. Ahmad, *J. Eur. Ceram. Soc.* **2020**, *40*, 3358.
[51] B. Cheng, H. Lou, A. Sarkar, Z. Zeng, F. Zhang, X. Chen, L. Tan, K. Glazyrin, H. P. Iiermann, J. Yan, L. Wang, R. Djenadic, H. Hahn, Q. Zeng, *Mater. Today Adv.* **2020**, *8*, 100102.
[52] M. Fracchia, P. Ghigna, T. Pozzi, U. Anselmi Tamburini, V. Colombo, L. Braglia, P. Torelli, *J. Phys. Chem. Lett.* **2020**, *11*, 3589.
[53] N. J. Usharani, R. Shringi, H. Sanghavi, S. Subramanian, S. S. Bhattacharya, *Dalton Trans.* **2020**, *49*, 7123.
[54] P. Ravikumar, B. Kisan, A. Perumal, *AIP Adv.* **2015**, *5*, 087116.
[55] D. Liu, D. Li, D. Yang, *AIP Adv.* **2017**, *7*, 015028.
[56] A. Gallo, C. Pirovano, P. Ferrini, M. Marelli, R. Psaro, S. Santangelo, G. Faggio, V. Dal Santo, *Appl. Catal., B* **2012**, *121*, 40.
[57] E. Lökçü, C. Toparli, M. Anik, *ACS Appl. Mater. Interfaces* **2020**, *12*, 23860.
[58] H. Chen, N. Qiu, B. Wu, Z. Yang, S. Sun, Y. Wang, *RSC Adv.* **2020**, *10*, 9736.
[59] S. Lee, A. M. Sastry, J. Park, *J. Power Sources* **2016**, *315*, 96.
[60] X. Li, X. Sun, X. Hu, F. Fan, S. Cai, C. Zheng, G. D. Stucky, *Nano Energy* **2020**, *77*, 105143.
[61] X. Lu, A. Bertei, D. P. Finegan, C. Tan, S. R. Daemi, J. S. Weaving, K. B. O'Regan, T. M. M. Heenan, G. Hinds, E. Kendrick, D. J. L. Brett, P. R. Shearing, *Nat. Commun.* **2020**, *11*, 2079.
[62] H. Wang, R. Qian, Y. Cheng, H. H. Wu, X. Wu, K. Pan, Q. Zhang, *J. Mater. Chem. A* **2020**, *8*, 18425.
[63] W. Xu, P. A. Russo, T. Schultz, N. Koch, N. Pinna, *Chem Electro Chem* **2020**, *7*, 4016.
[64] K. M. Daniels, S. Shetu, J. Staser, J. Weidner, C. Williams, T. S. Sudarshan, M. V. S. Chandrashekhar, *J. Electrochem. Soc.* **2015**, *162*, E37.
[65] T. X. Nguyen, C. C. Tsai, J. Patra, O. Clemens, J. K. Chang, J. M. Ting, *Chem. Eng. J.* **2022**, *430*, 132658.
[66] M. Fiore, G. Longoni, S. Santangelo, F. Panto, S. Stelitano, P. Frontera, P. Antonucci, R. Ruffo, *Electrochim. Acta* **2018**, *269*, 367.
[67] S. Santangelo, M. Fiore, F. Pantò, S. Stelitano, M. Marelli, P. Frontera, P. Antonucci, G. Longoni, R. Ruffo, *Solid State Ion* **2017**, *309*, 41.

[68] R. Kim, D. Choi, K. Y. Shin, D. Han, *J. Alloys Compd.* **2021**, *879*, 160416.
[69] I. Ryu, J. W. Choi, Y. Cui, W. D. Nix, *J. Mechanics Phys. Solids* **2011**, *59*, 1717.
[70] Z. Huang, H. Gao, Z. Yang, W. Jiang, Q. Wang, S. Wang, J. Ju, Y. U. Kwon, Y. Zhao, *Mater. Des.* **2019**, *180*, 107973.
[71] A. Ponti, M. H. Raza, F. Pantò, A. M. Ferretti, C. Triolo, S. Patanè, N. Pinna, S. Santangelo, *Langmuir* **2020**, *36*, 1305.